Interfacial reaction between ZrNbHfTa foil and graphite: Formation of high-entropy carbide and the effect of heating rate on its microstructure

Interfacial reaction between ZrNbHfTa foil and graphite: Formation of high-entropy carbide and the effect of heating rate on its microstructure

Mattia Biesuz [a, b, *], Theo G. Saunders [a], Kan Chen [a], Mauro Bortolotti [b], Milena Salvo[c], Salvatore Grasso [d], Michael J. Reece [a]

[a] Queen Mary University of London, School of Engineering and Materials Science, Mile End Rd., London E1 4NS, UK

[b] University of Trento, Department of Industrial Engineering, Via Sommarive 9, Trento 38123, Italy

[c] Politecnico di Torino, Department of Applied Science and Technology, Turin 10129, Italy

[d] Key Laboratory of Advanced Technologies of Materials, Ministry of Education, School of Materials Science and Engineering, Southwest Jiaotong University, Chengdu 610031, China

* Corresponding author: M.B. mattia.biesuz@outlook.com

Abstract

The interfacial reaction between graphite and a ZrNbHfTa foil using a spark plasma sintering (SPS) machine was studied. The interlayer was converted during the treatment into a high-entropy carbide by the reaction between the alloy and the graphite substrate. The degree of conversion depended on the processing time and temperature, but could be completed in only 16 s using the flash-spark plasma sintering process.

The final microstructure was strongly influenced by the heating rate. Flash-SPS processing (heating rate about 120 °C/s) melted the alloy, which is then squeezed and deformed before its conversion to the high-entropy carbide (Zr,Nb,Hf,Ta)C. On the contrary, when conventional heating was used (i.e., 10 °C/min) the metal reacted with the graphite substrate before it melted. This concept appears to be generally applicable to different graphite/metal systems, with particular implications in the fields of graphite/metal joining.

1. Introduction

Since 2015 there is an increasing interest in high-entropy ceramics [1–10], as they possess intriguing properties as a consequence of their multi-element composition, e.g., giant dielectric constant [3]; Li ion super-ionic conductivity [11]; catalytic CO oxidation [12]; soft magnetic properties [9]; and enhanced mechanical properties [10,13]. High-entropy carbide (HEC) solid solutions are of particular interest [13–19]. It has recently been shown that the quaternary carbide (Zr,Nb,Hf,Ta)C possess mechanical properties that surpass those of the single element or binary carbides, including hardness [13] and yield and failure strength [10]. However, the formation of (Zr,Nb,Hf,Ta)C has only been studied by solid state reaction starting from the mono-element

carbides. This processing route presents some limitations, as the commercial carbide powders are often contaminated with oxygen (due to the carbothermal reduction process being incomplete). The presence of oxygen contamination is very deleterious for high temperature properties, which are of primary importance for such refractory compounds. On the other hand, an alternative processing route could involve the formation of (Zr,Nb,Hf,Ta)C starting from a metal alloy and graphitic carbon, which has not been investigated to date.

A deeper understanding of the reaction between high-entropy alloys (HEAs) and graphite finds other specific motivations. As a matter of fact, the development of joining processes for ceramics is of great technological interest [20–28] because it enables the production of large and complex components by assembling small and simple parts. Some HEAs have exceptional mechanical properties [29], some of them are also extremely refractory [30], thus they are of particular interest for high temperature structural applications. On the other hand, graphite stands as one of the most refractory compounds when considering ceramics working in inert environments. On this basis, the development of HEAs / graphite joints is of some interest. Graphite is usually bonded using metallic carbide-forming interlayers [31–33], whose reaction with graphite itself ensures adhesion. Hence, an investigation of the carbon to metal reaction in high-entropy systems is a starting point for the development of novel graphite to high-entropy alloy joints.

On the other hand, the recent advent of flash sintering (FS) [34–37] and of flash-spark plasma sintering (FSPS) [38,39] has opened up new opportunities in the field of ceramic processing. During the flash event the sample is rapidly heated under the effect of an external electric current by the Joule effect [40] and sinters in just a few seconds at a relatively low temperature. Albeit the mechanisms behind the flash are still being debated [41–50] (because of the intrinsic difficulty in decoupling thermal and athermal effects), it is clear that extremely rapid diffusion and mass transport are involved. These phenomena are integral not only to sintering, but they also apply to flash-like processes in different fields of ceramic processing ranging from synthesis [51,52] to solid state reactions [53–55], from glass softening [56,57] to joining [58–63]. In this field the recent work by Gild et al. is of interest: it proves that high-entropy carbides and borides can be manufactured within 2 min by reactive FSPS [64].

~~In this work we investigated~~ The objective of this work was to investigate the reaction between graphite and a ZrNbHfTa alloy foil using a spark plasma sintering (SPS) machine. The rationale behind the choice of the alloy is based on the followings: (i) it is a precursor for (Zr,Nb,Hf,Ta)C, which has interest because of its exceptional mechanical properties [10,13]; group 4 and 5 elements produce high-entropy alloys with high ductility and mechanical strength [65][66]; (iii) all of the elements in the alloy composition produce extremely refractory carbides with melting temperature higher than 3500 °C (except V and Ti whose carbides melt below 3200 °C). In this work, we were aimed to answer the following questions:

i. Does a high entropy carbide form from the reaction between a ZrNbHfTa alloy and graphite?
ii. How does the alloy to carbide conversion proceed? At what temperature? Is the

transformation homogeneous or is there segregation?

iii. Is there an effect of the heating rate on the transformation?

To answer these question, treatments with relatively low (10 °C/min, spark plasma sintering, SPS) and extremely high heating rates (120 °C/s, flash spark plasma sintering) were investigated ~~in order to highlight the effect of the heating rate on the interlayer deformation and reactivity~~. The controlled formation of (Zr,Nb,Hf,Ta)C from the reaction between the alloy and the graphite has two important implications for future research activities: (i) it opens up a new processing route to produce ~~high-purity~~ high-entropy carbides without using single element carbide powders as raw materials (often contaminated with oxygen); and (ii) provides a preliminary study toward the development of HEA/graphite joints with HEC interface.~~ novel approach to metal/graphite joining.~~

2. Experimental procedures

Wires (diameter = 1 mm) of the mono-element metals were purchased from Goodfellows and served as the raw materials for the production of the ZrNbHfTa alloy: Zr (ZR005143, purity 99.2%); Nb; (NB005130, purity 99.9%); Hf(HF005130, 97%); Ta(TA005160, purity 99.9%). An appropriate amount of each wire was cut from the coils in order to obtain 0.33 g of the equimolar alloy. The four mono-element wires were then arc melted using a commercial welding machine (Jasic tig500p AC/DC used in DC) in an Ar atmosphere on a water-cooled copper plate. The melting procedure was repeated at least five times to homogenize the material composition.

The buttons obtained after arc melting were then hand-hammered at room temperature to produce foils with a cross-section of about 110 mm^2 to 120 mm^2 (foil thickness around 270 µm). The foils were then polished; reaching a final average thickness of between 150 µm and 190 µm.

The ZrNbHfTa foil was introduced between two graphite disks (grade Durograph 20 of 3 mm thickness and 20 mm in diameter; density = 1.84 g/cm^3; open porosity = 10%; electrical resistivity 14 µΩ m) and then joined using a SPS system (HPD 25/1, FCT systems, Germany). A load of 5 kN was maintained during the process; the atmosphere was Ar (0.01 atm). The temperature was measured using a pyrometer focused on the hollowed graphite punch at 4 mm from the sample.

Two different treatment procedures were employed. The first one, named flash, involved extremely rapid electric heating (about 120 °C/s) of the components. Here, the power of the SPS system was set to 100% of its maximum output; which corresponds to about 9.3 V output at the SPS diodes and ~6.5 V on the SPS punches (heating power around 18 to 19 kW). The electric power was applied for different times, ranging between 10 s and 16 s, followed by free cooling. The second procedure involved the same die less arrangement but using a relatively slow heating rate (SPS). In this case the heating rate was fixed at 200 °C/min up to 1600 °C, followed by slow heating at 10 °C/min up to two different target temperatures, 1900 °C and 2200 °C. The maximum temperature was maintained for 30 s and then the sample was cooled at 200 °C/min.

After the treatment, the samples were cut orthogonally to the foil and polished using SiC papers (down to 4000 grit) and diamond pastes (down to 1 μm grain size). The cross-section was then analyzed by SEM/EDS using a FEI Inspect-F instrument.

The phase analysis of the starting alloy and of the joint interlayer was carried out using XRD (PANalytical Xpert-Pro diffractometer in the 2θ range 20° to 70°, radiation Cu kα). Preferred orientation measurements were performed by using a Huber 4 circle texture diffractometer equipped with a microfocus 50 W Cu source, a two-dimensional elliptic mirror monochromator and a Dectris Eiger 1M 2D hybrid pixel detector. The samples were positioned in a reflection geometry; diffraction spectra were collected over the 20° to 120° 2θ range and χ axis (0° to 45°, 15° step) and ϕ axis (0° to 360°, 30° step) for a total of 48 sample orientations. Full profile Rietveld analysis was performed using the Maud software [67] by adopting a standard isotropic size/strain broadening model [68] and the WIMV method for preferred orientation quantitative analysis [69]. In order to investigate the phase composition of the interlayer, one of the two joined graphite disks was carefully removed by grinding (using 800 grit diamond paper), thus the diffraction occurred on the interlayer plane. The same samples were also analyzed using a Nexsa X-Ray Photoelectron Spectrometer (XPS) system. To remove surface contamination, the samples were ion-milled for 3 min using 4 keV ions.

Finally, in order to estimate the melting temperature of the alloy, an arc melted sphere was introduced into a pressure-less SPS system (sketch available in ref. [70]) and placed on a graphite disk. The temperature was increased at a rate of 100 °C/min, and its evolution was monitored using the top pyrometer of the SPS system pointed at the metal sphere. When the melting temperature was reached a deviation in the time vs. temperature plot was observed because of an abrupt change in the sample emissivity/roughness and because of the melting enthalpy. To calibrate the system the same experiment was carried out using metals of known melting point (i.e., Zr and Ta).

3. Results and discussion

Fig. 1 reports the XRD spectra of the arc melted alloy before and after forging. The spectra showed that the material was substantially single phase with *bcc* structure and lattice parameter of 3.4343 Å (the phase is identified as *A* in Fig. 1). A weak signal associated with a secondary *bcc* phase with lattice parameter 3.2968 Å (highlighted by the arrows in Fig. 1) was also detected before forging. The as arc melted alloy did not present any texture and no significant broadening of the diffraction peaks was observed. The *bcc* crystal structure of ZrNbHfTa was analogous (except for the difference in cell parameter) to the one of the well-known high-entropy TiZrNbHfTa alloy [71–75]. The formation of a *bcc* solid solution was not surprising considering the crystal structure of the metals in its composition. Ta and Nb are *bcc* from room temperature up to their melting point, whereas Zr and Hf, although being *hcp* at room temperature, convert to *bcc* at 863 °C and 1749 °C [73], respectively. Thus, all of the metals are stable as a *bcc* phase at least at high temperature. The presence of a very small amount of a secondary *bcc* phase with smaller cell parameter

(highlighted by arrows in Fig. 1) could be attributed to a partial lack of homogeneity in the melt. It seems that the peak shift and related cell parameter variation is too large to be explained in terms of microsegregation during solidification, which has been reported in cast TiZrNbHfTa [71,74,76]. ~~to microsegregations during solidification. Microsegregation in cast TiZrNbHfTa had been previously reported [71,74], where Nb and Ta (V group, high melting T elements) segregate into the dendrites, whereas Ti, Zr and Hf (IV group, lower melting temperature) segregate into the inter dendritic region [71,74].~~

Fig. 1(c) shows that the forging process caused the development of strong texture with the crystallographic direction <2 0 0> oriented orthogonally to the forged foil plane, whereas the as arc melted samples exhibit only very weak texture (Fig. 1(b)), probably due to the solidification process. The deformation also leaded to significant peak broadening, which could be accounted for by an isotropic size/strain model; refined values for the average volume-weighted crystallite size and r.m.s. microstrain are 22 nm and 4.54 x 10^{-3}, respectively. Moreover, the secondary phase disappeared after forging. This was likely due to the heavy plastic deformation destroying the structural inhomogeneities and the solidification microstructures ~~solidification dendritic structures and the corresponding microsegregation~~ (mechanical alloying).

Fig. 2(a) shows the temperature vs. time plots measured by the SPS top pyrometer for the alloy in the pressure-less SPS configuration. The deviation from the linear plot is associated with the alloy melting. This gave an estimated melting temperature of the alloy of around 2060 °C (Fig. 2(d)), after calibrating the system using metals of known melting temperature (Fig. 2(b,c)).

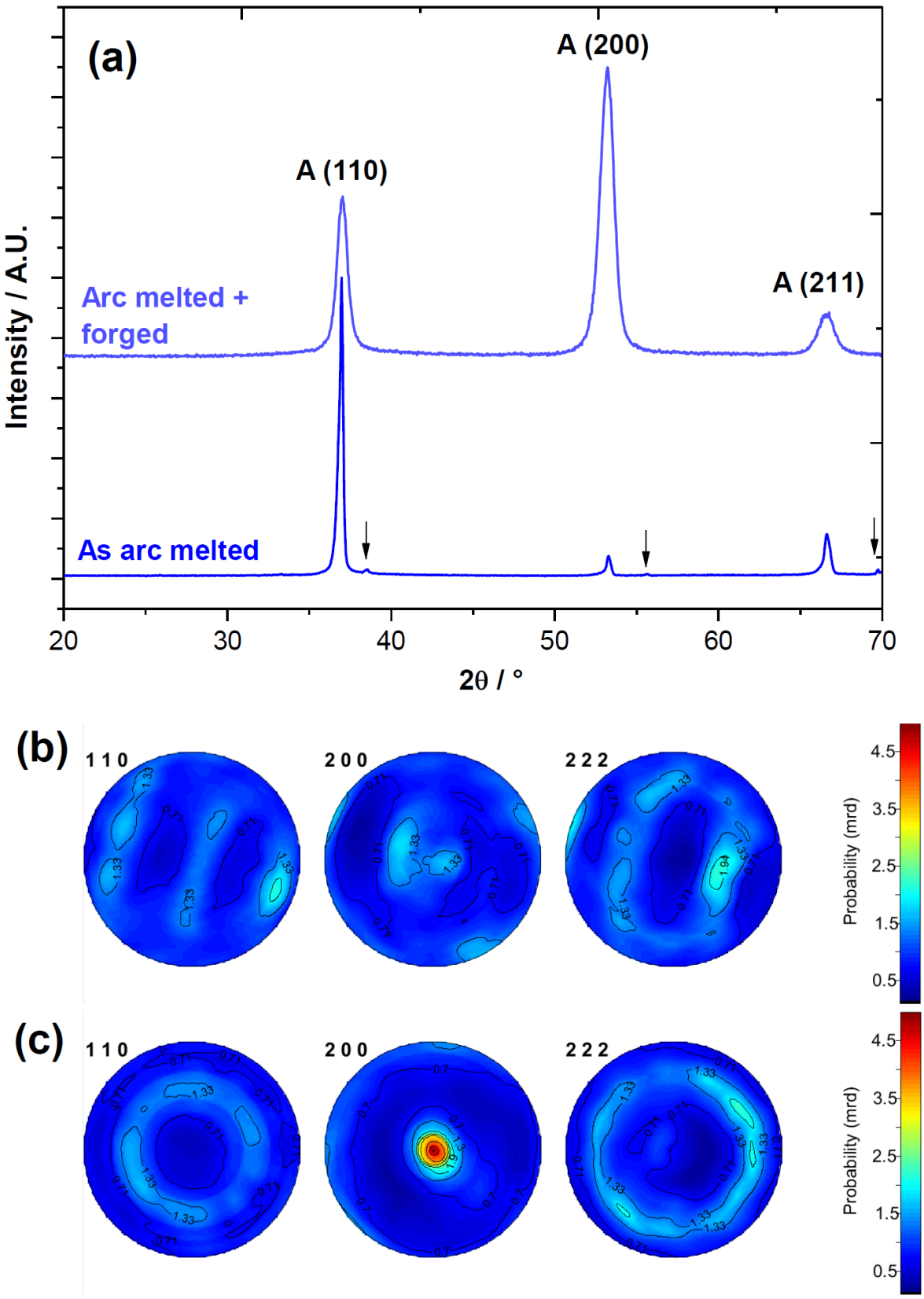

Fig. 1. (a) XRD spectra of the as arc melted and forged ZrNbHfTa alloy. "*A*" represent the main *bcc* phase with lattice parameter 3.4343 Å. The arrows indicate a secondary *bcc* phase with lattice parameter of 3.2968 Å. Reconstructed pole figures of both samples: (b) the as arc melted sample

exhibits only a weak solidification texture; (c) the forged sample shows the development of strong preferred orientation of the <2 0 0> direction orthogonal to the foil plane.

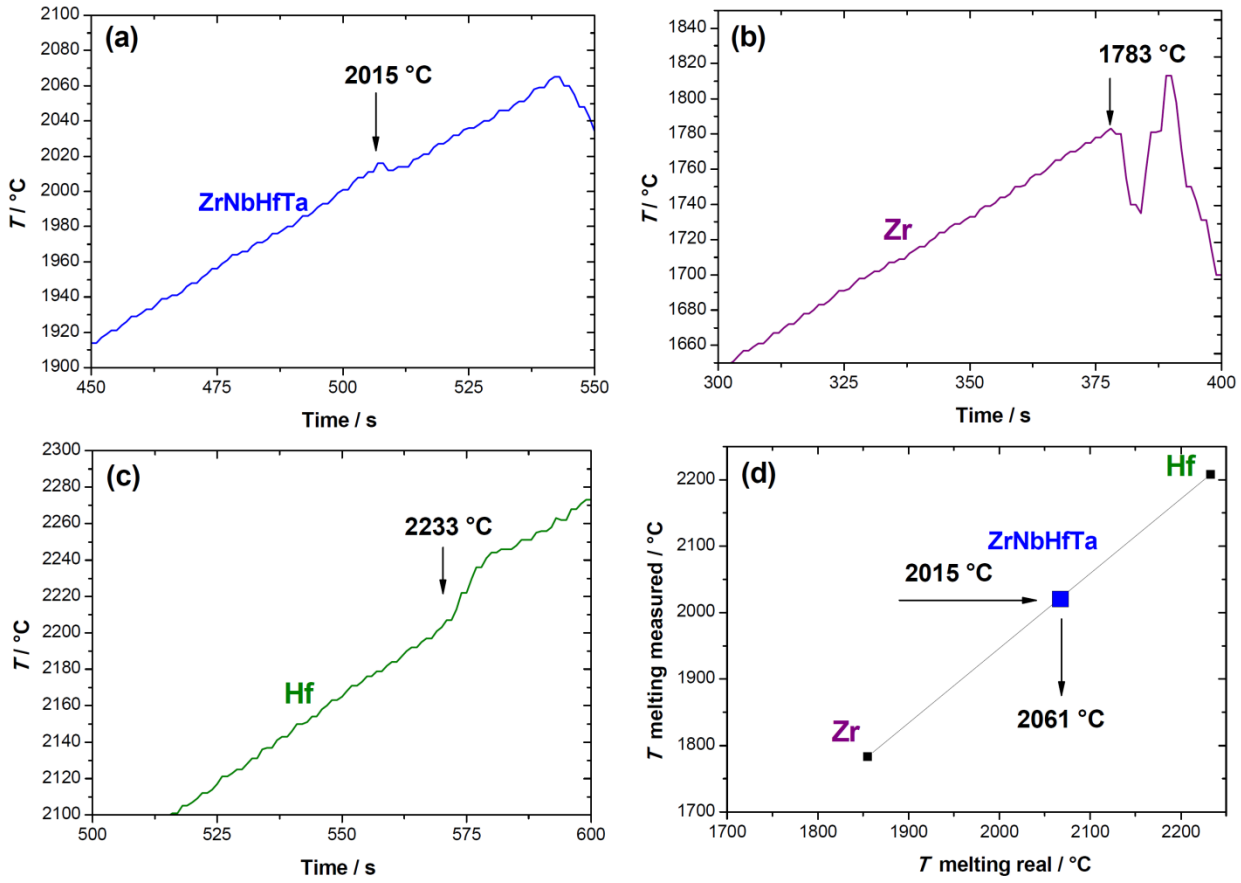

Fig. 2. Temperature (as measured by the SPS top pyrometer) vs. time plot while heating in pressure-less conditions at 100 °C/min: (a) the quaternary alloy; (b) Zr; and (c) Hf. The deviation from the linear plot represents the sample melting. The calibration of the measurement (done using the known melting temperature of Zr and Hf) is reported in (d).

The temperature evolution during the graphite/alloy reaction is reported in Figs. 3(a) and (b) for the SPS and flash treatments, respectively. One can observe that the flash treatments produced extremely high temperatures in just a few seconds (10 s to 16 s) with heating rates of the order of 120 °C/s, whereas the cooling required several tens of seconds/few minutes. The peak temperatures measured by the top pyrometer for the different flash processes is summarized in Table 1. These ranged between 1705 °C and 2233 °C for samples treated for 10 s and 16 s, respectively. However, due to the extreme conditions generated during the flash treatment, the real temperature at the interface was likely to be several tens of degrees higher than the one measured by the top pyrometer (4 mm from the sample).

Except for the flash process carried out for 10 s, in all other cases the graphite samples were stuck together after their treatments. Hence, in most of the cases a joint between the graphite and the

quaternary interlayer was achieved in just a few seconds. However, a preliminary mechanical characterization of the interface of the samples flashed for 16 s revealed that they only had limited mechanical strength (few MPa of shear strength, as reported in "Supplementary material"). This was likely due to the generation of thermal stresses during the high temperature process(~ 2000 °C). Possible routes to overcome this limitation might involve modification to the thermal treatment; i.e., using lower cooling rates or reducing of the joining temperature by employing longer treatments.

The key microstructural differences between the slow heating (SPS) and fast heating (flash) processes are highlighted in Fig. 4 and Table 1. We can infer that the thickness of the interlayer was greatly decreased during the flash process, whereas it remained almost unchanged during the SPS one (in other words if the heating rate is slow the foil remains intact). In particular, the foil thickness after flash (t_1 in Table 1) was reduced to about 45%, 30% and 10% of the initial one (t_0 in Table 1) for the 12 s, 14 s and 16 s treatments, respectively. Moreover, in the case of rapid heating (flash) the metal infiltrated the graphite porosity (additional micrographs and EDS maps showing that infiltration occurred are reported in Figure S1 – S7, "Supplementary material"). This showed that the rapid heating processing produced microstructures that were not possible under standard heating conditions. In particular, in the samples produced by flash the metal melted, causing a decrease of the interface cross-section and a migration of the alloy into the graphite porosity. Looking at the peak temperature recorded by the top pyrometer (Table 1), melting was achieved for the samples treated for 14 s and 16 s, whereas it might not have been achieved for the one treated for 12 s.

It was quite surprising that the sample treated with slow heating (SPS) at 2200 °C was still substantially undeformed and no infiltration was visible, even though the treating temperature abundantly surpassed the melting point of the alloy. Considering the slow heating process we were not expecting significant errors in the temperature measurement for the SPS configuration. Hence, we deduced that the interlayer actually changed its properties during the slow heating process or, in other words, it reacted with graphite forming carbides before reaching the melting point.

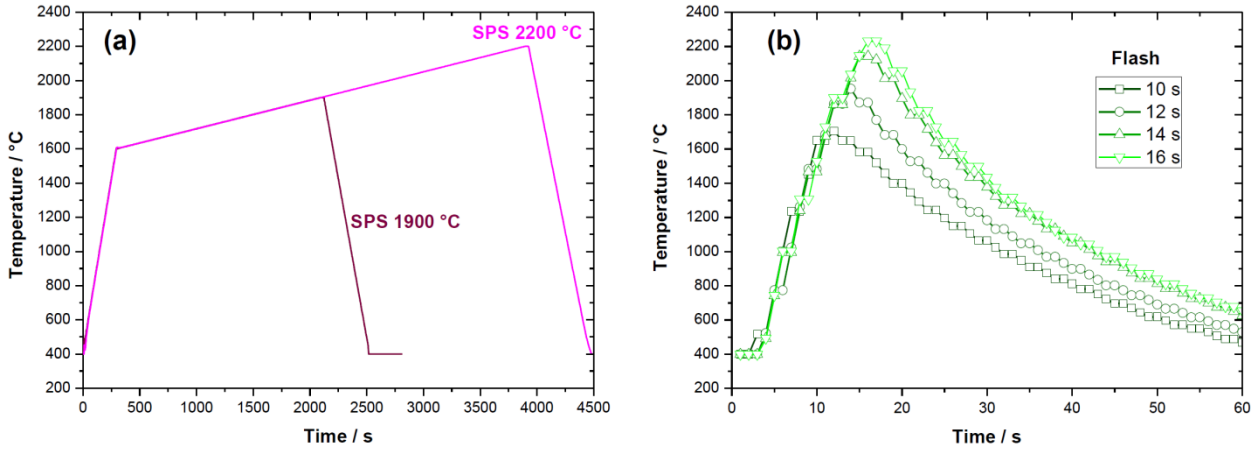

Fig. 3. Temperature evolution measured by the top pyrometer of the SPS system pointing at the hollowed graphite punch at 4 mm form the sample for: (a) SPS; and (b) flash treatments.

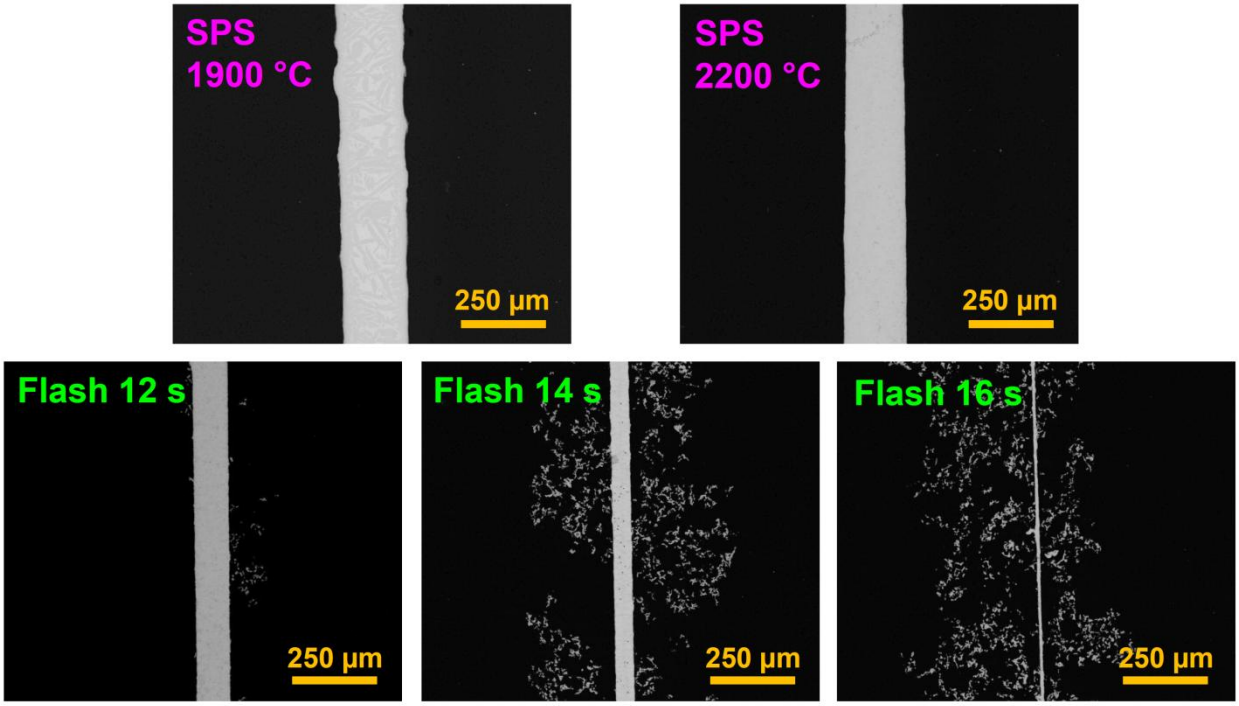

Fig. 4. SEM backscattered electron micrographs of the interlayer cross-section (the black regions are the graphite substrates, the grey one is the interlayer).

Table 1. Summary of the key results for the different joining processes. The thickness "t_0" is the average ZrNbHfTa foil thickness before joining as calculated from the foil density (ρ), mass (m) and cross-section (S): $t_0 = m/\rho S$, whereas "t_1" is evaluated by SEM micrographs (Fig. 4) after joining. * N.M. stays for "Not Measured".

Treatment	Peak T/°C	Joined	Infiltration in graphite	t_0/µm	t_1/µm
SPS 1900 °C	1900	Yes	No	164	150 – 210
SPS 2200 °C	2200	Yes	No	185	150 – 190
Flash 10 s	1705	No	No	157	N.M.*
Flash 12 s	1963	Yes	Yes	171	60 – 100
Flash 14 s	2144	Yes	Yes	164	40 – 60
Flash 16 s	2233	Yes	Yes	177	10 – 30

In order to investigate the formation of carbides during processing, we characterized the structure/microstructure of the interphase using XPS, SEM, EDS and XRD. Whereas SEM and EDS were operated on cross-sections orthogonal to interlayer plane, XRD and XPS were carried out directly on the interlayer plane (after having grounded down one of the two graphite disks to

reveal it).The XPS spectra revealed a clear shift in the binding energies for the different metals in the alloy composition during the treatments (Figs. 5(a-d)). In particular, the photoelectrons emission peaks associated with the Zr *3d*,Nb *3d*, Ta *4f* and Hf *4f* orbitals all shifted to higher energies as a result of the thermal treatments. No significant differences could be seen between the samples Flash 16 s and SPS 2200 °C. The binding energy shift was consistent with the formation of Zr-C, Nb-C, Ta-C and Hf-C bonds, thus indicating the formation of the carbides [77–85]. Additionally, the reaction between the metals and graphite was confirmed by the C *1s* spectrum, which has a strong signal at 282.45 eV for the thermally treated samples (Figs. 5(e)). This was related to the formation of M-C bonds; as a matter of fact the binding energies reported in the literature for Zr-C, Nb-C, Ta-C and Hf-C bonds are 281.6 eV [85], 282.9 eV [79], 282.9 eV [82] and 282.5 eV [84], respectively. Hence, the measured peak at 282.45 eV was in perfect agreement with C atoms in a mixed environment containing the different metals in the alloy composition. The signal at about 284.8 eV was associated with graphite contamination (residual unreacted graphite from the substrate) [84].

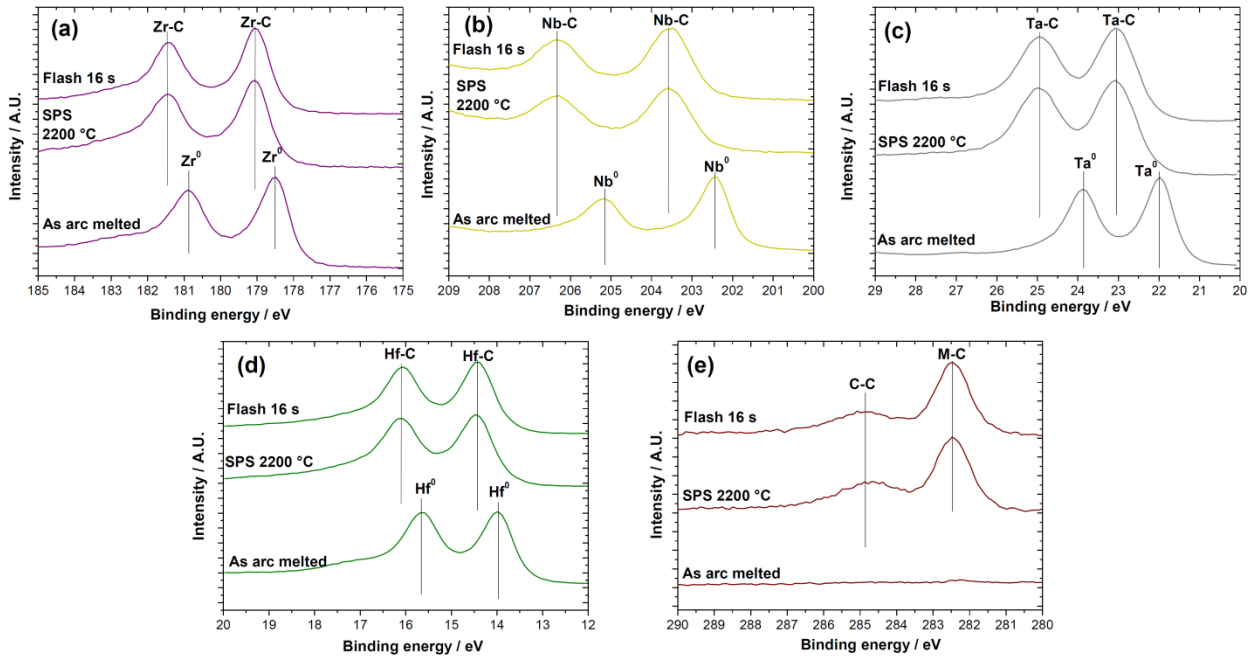

Fig. 5. XPS spectra before and after the Flash 16 s and SPS 2200 °C treatments for: (a) Zr *3d*; (b) Nb *3d*; (c) Ta *4f*; (d) Hf *4f* ; and (e) C *1s*.

The panel in Fig. 6 and Table 2 list the key microstructural features of the interlayer after SPS processing. The interlayer treated at 1900 °C was biphasic, being constituted by a *bcc* and a *fcc* phase (*rock salt*) identified as *A'* and *F*, respectively. From the XRD data (obtained on sample ground down to reveal interlayer), the cell parameter of the two phases were 3.3317 Å and 4.5767 Å, respectively. Hence, the cell parameter of *A'* was substantially smaller than the one of the parent *bcc* alloy (*A*). The phase *F* matched the diffraction spectra of the carbide solid solution as reported in [13], thus we could attribute *A'* to the remaining unreacted alloy and *F* to the carbide.

The carbide phase in the SEM micrographs in Fig. 6 could be identified because of the Z-contrast in the backscattered electron imaging, where the carbide was the darker phase because of its lower average atomic number. The carbide developed inside the *A'* matrix in the form of elongated crystals, which are visible along all of the interlayer cross-section. A region clearly more rich in *F* could be identified at the interface between the interlayer and the graphite. This was consistent with the attribution of *F* to the carbide formed by the reaction between graphite and the alloy interlayer; as a matter of fact, the carbide was expected to form starting from the interface between the two reagents.

One can also observe that the chemical composition of the two phases was different, where *A'* was richer in Nb and Ta while *F* contained mainly Zr and Hf (Fig. 6). To understand such differences in the chemical composition between *F* and *A'* one can consider the thermodynamics of the carbide formation. Fig. 7 reports the free energy for carbide formation as a function of the temperature (thermochemical data taken from [86]). It evidences that Zr and Hf have a higher affinity to carbon, with a larger negative energy of formation of the single-element carbides. Therefore, the first carbide formed from the quaternary alloy was richer in these two elements. This indeed caused Ta and Nb enrichment in the unreacted alloy (*A'*). If we consider the atomic radii of the different metals (R_m in Fig. 7), we can also observe that the *A'* phase contained a higher load of the atoms with the smallest atomic radius. This caused a shrinkage of the unit cell of the alloy (Table 2) and a displacement to higher angles of its XRD reflections with respect to the parent *A* phase (Fig. 6). Elemental segregations due to the different formation energy of the carbides in other high-entropy alloys has already been reported as for the case of: $Fe_{40.4}Ni_{11.3}Mn_{34.8}Al7.5Cr_6$ [87], $Al_{0.5}CrFeNiCo_{0.3}C_{0.2}$ [88] and CoCrFeMnNi [89] alloys, where Cr rich carbide formed.

On the contrary, in the sample treated at 2200°C the interlayer was a single phase solid solution carbide. In this case, as shown in the EDS maps in Fig. 6, the distribution of all of the constituent elements was homogeneous. Moreover, the cell parameter of *F* slightly decreased with increasing treating temperature from 1900 °C to 2200 °C (Table 2). These results were consistent with a complete reaction of the alloy with graphite to form a pure high-entropy carbide interlayer. The cell parameter change was due to the change in the carbide composition (rich in Zr and Hf at 1900 °C, equimolar at 2200 °C).

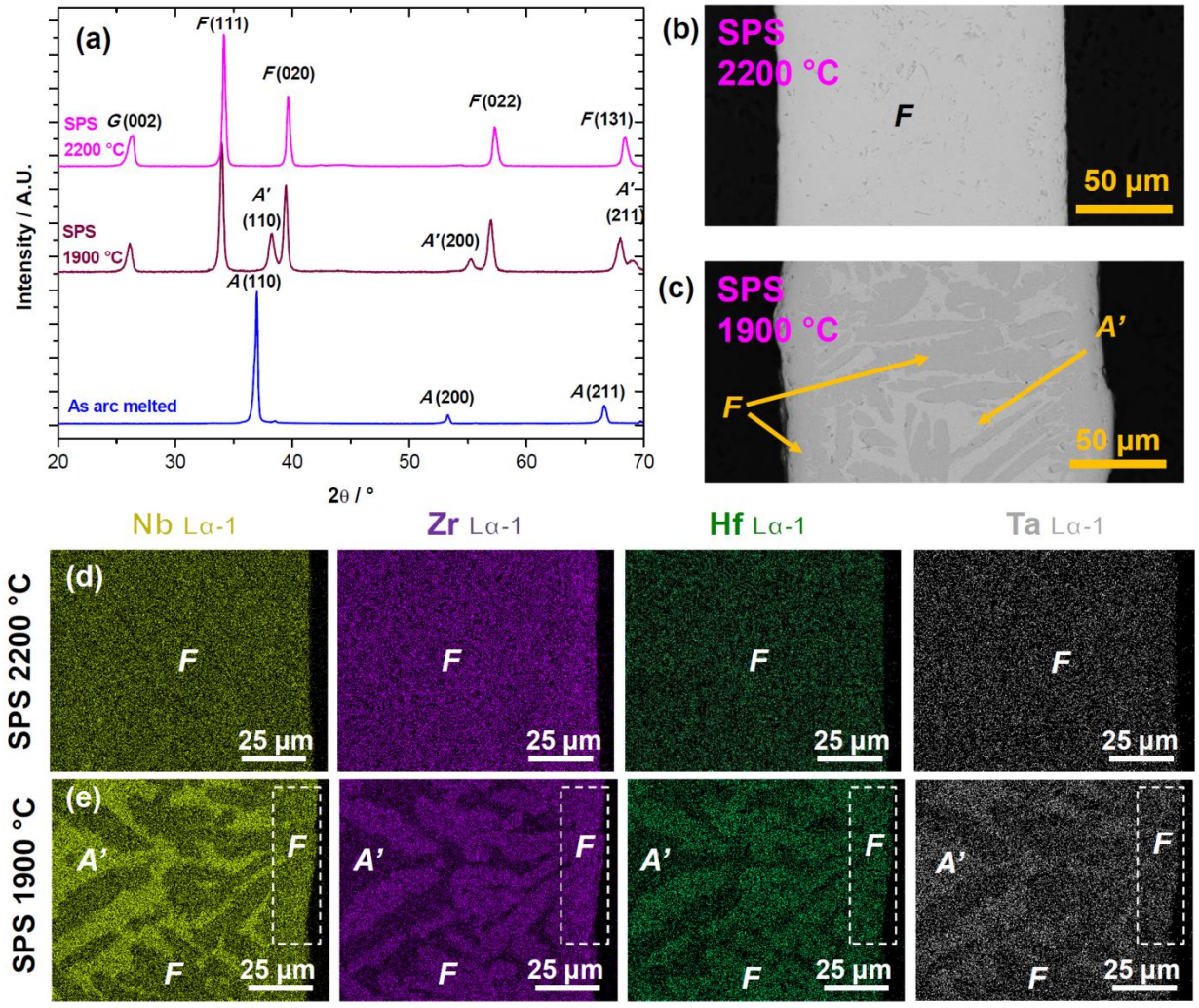

Fig. 6. (a) XRD spectra (Cu Kα radiation), (b, c) SEM micrographs, and (d, e) EDS mapping of the interlayer region of the samples produced by SPS. The different phases identified by XRD (i.e, *A'* and *F*) are highlighted in the micrographs and in the EDS maps. The white dashed line rectangles identify *F* (carbide) rich regions close to graphite. The phase *G* in the XRD pattern represents the reflection of the graphite substrate.

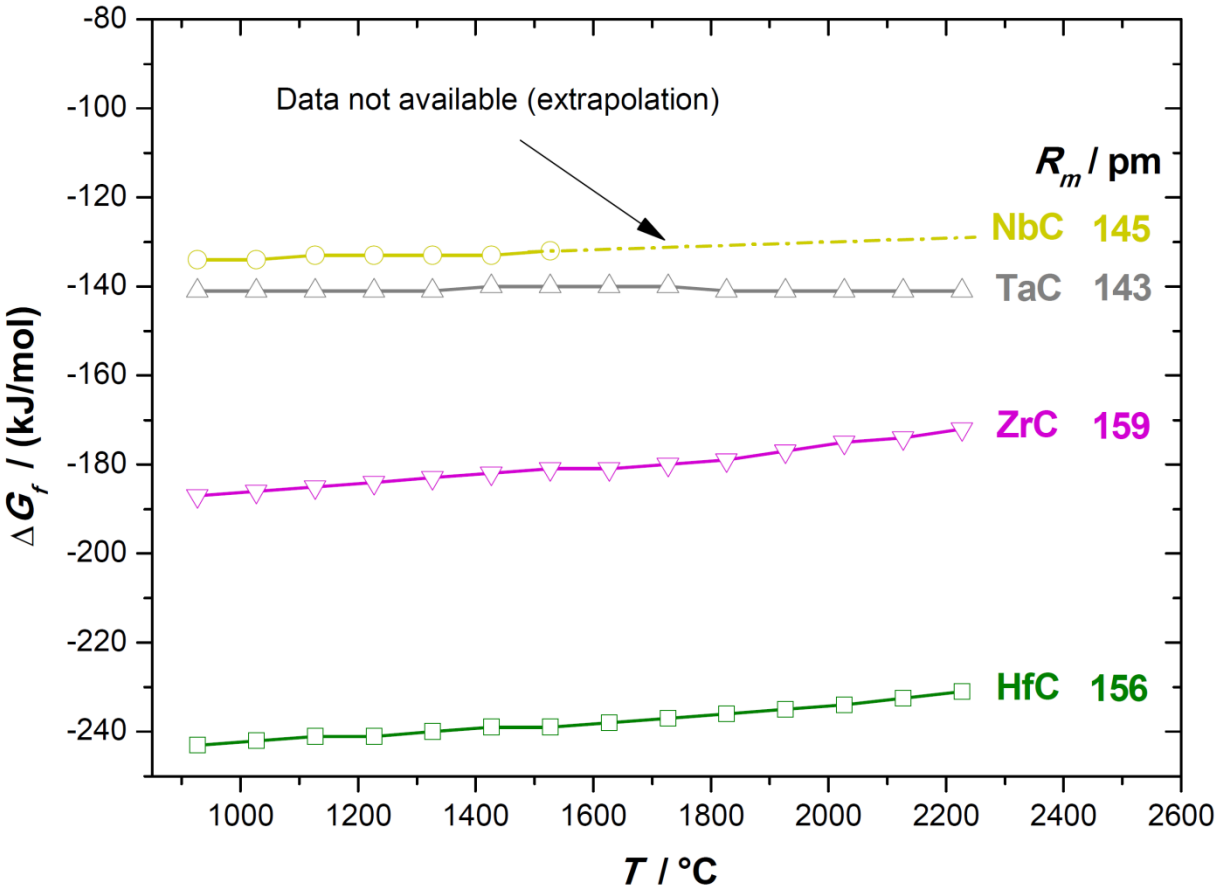

Fig. 7. Ellingham diagram representing the Gibbs' free energy of formation of the different carbides (data refers to 1 mole of carbide). Thermochemical data taken from [86]. R_m is the atomic radius of the different metals, data taken from [13].

The panel in Fig. 8 and Table 2 present the characteristics of the interlayer produced by flash processing. The samples treated for 10 s, 12 s and 14 s were biphasic, where diffraction peaks associated with the parent alloy (*A*) and to the rock salt carbide (*F*) were present. The amount of *F* increased with the discharge time (Table 2), meanwhile the lattice parameter of *A* slightly decreased (Table 2). The first formed carbide, as in the case of SPS samples, was more concentrated close to the interface between the interlayer and the graphite substrate. Its chemical composition differed from the equimolar parent alloy and was rich in Hf and Zr. This is evidenced by the EDS spot analysis in Fig. 8 for the case of the sample Flash 12 s (also representative of Flash 14 s). Additional SEM micrographs and EDS maps can be found in "Supplementary material" (Figure S1 - S7).

The sample treated for 16 s, which reached the highest temperature during processing (Table 1), was single phase and contained only the carbide. However, the diffraction peaks presented an irregular shape and were very broad. Moreover, the chemical composition measured by EDS mapping (Fig. 8) was not completely homogeneous (i.e., it seemed that Ta had segregated in the

interlayer center, whereas Hf was more abundant close to the graphite). These segregations were indeed at the origin of the observed diffraction peak broadening, which could be modeled as a rock salt phase with a cell parameter distribution with two maxima located at 4.6105 Å and 4.5588 Å. The origin of the chemical inhomogeneity resided in the elemental segregations during the carbide formation. As it was shown before, some elements (i.e., Hf and Zr) had a higher affinity for carbon and were concentrated in the initially formed carbide. This was more abundant at the graphite/metal interface, hence such elements tended to segregate close to the graphite, whereas the unreacted metals (i.e., Nb and Hf) concentrated in the interlayer center. Since the flash process was extremely rapid (and metal diffusion in carbides is very slow compared to carbon), there was no time for a complete homogenization under the effect of the concentration gradients and some segregations remained visible at the end of the process.

The above results highlight that the heating rate had a significant impact on the interlayer microstructure. It was clear that in the case of SPS (10 °C/min) the metal to carbide conversion is completed before reaching the melting point of the metal. Hence, it was not possible to squeeze/deform the metal interlayer and produce any infiltration into the graphite. On the contrary, the flash processes (about 120 °C/sec) produced complete melting of the alloy before it had time to react with graphite. It was thus possible to infiltrate the graphite by squeezing the molten metal interlayer, the reaction to form the carbide then took place. This concept is rather general and can probably be applied in the case of using different metallic interlayers to join graphite.

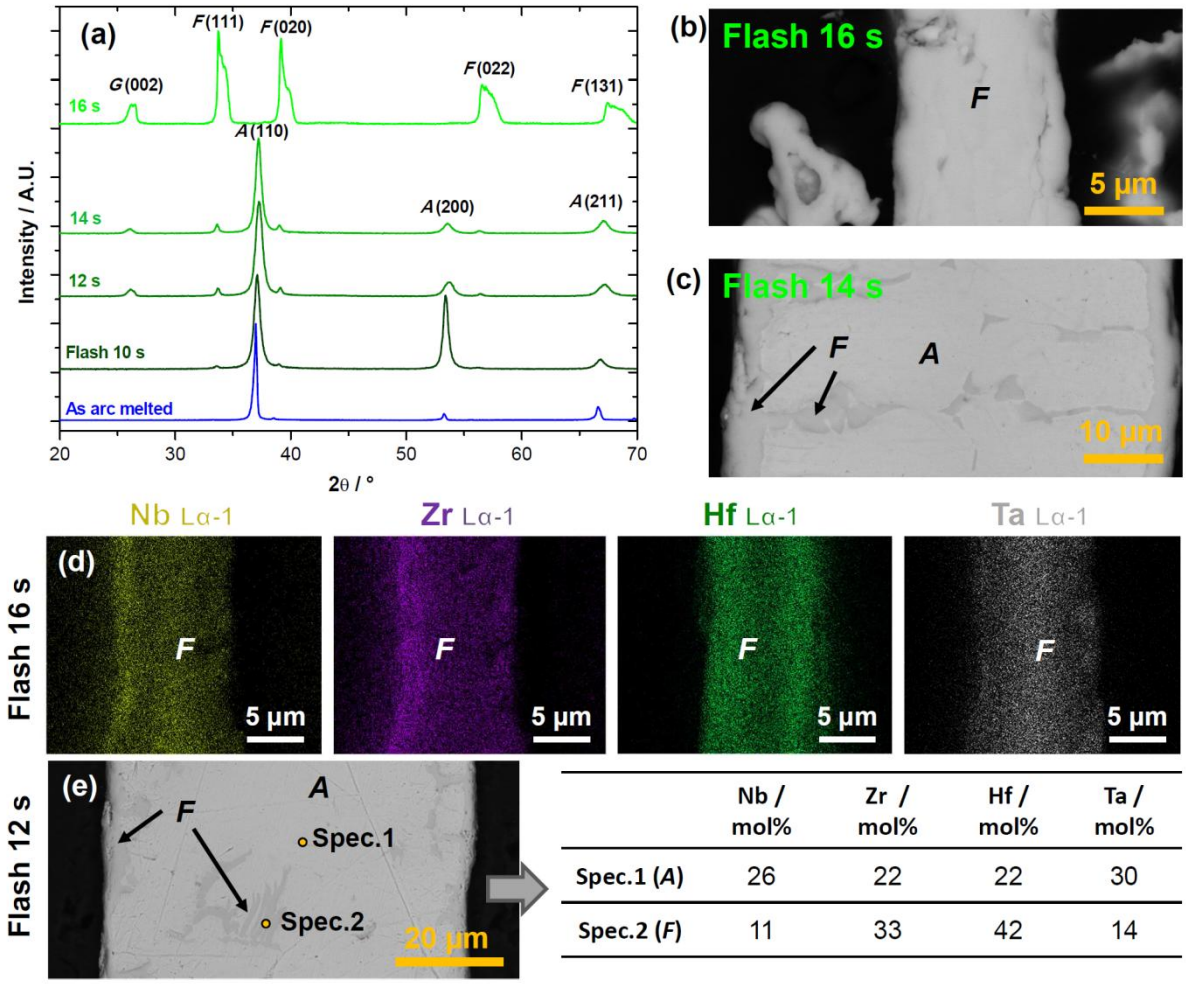

	Nb / mol%	Zr / mol%	Hf / mol%	Ta / mol%
Spec.1 (*A*)	26	22	22	30
Spec.2 (*F*)	11	33	42	14

Fig. 8. (a) XRD spectra (Cu Kα radiation), (b, c) SEM micrographs, and (d) EDS maps and spot (e) analysis of the joint region of the samples produced by flash. The different phases identified by XRD (i.e, *A* and *F*) are highlighted in the micrographs and in the EDS maps. The phase *G* in the XRD pattern represents the reflection of the graphite substrate.

Table 2. Summary of the key information extracted from the XRD spectra (Figs. 1, 6 and 8). "*a*" is the cell parameter.

Treatment	Phases	*A* (*bcc*)		*A'* (*bcc*)		*F* (*rock salt, fcc*)	
		Compo./wt%	*a*/Å	Compo./wt%	*a*/Å	Compo./wt%	*a*/Å
As arc melted	*A, A'*	99.0	3.4343	1.0	3.2968	-	-
Forged	*A*	100.0	3.4560	-	-	-	-
SPS 1900 °C	*A', F*	-	-	35.1	3.3317	64.9	4.5767
SPS 2200 °C	*F*	-	-	-	-	100.0	4.5500
Flash 10 s	*A, F*	99.8	3.4330	-	-	0.2	4.6274
Flash 12 s	*A, F*	97.3	3.4179	-	-	2.7	4.6130
Flash 14 s	*A, F*	95.7	3.4208	-	-	4.3	4.6200
Flash 16 s	*F*	-	-	-	-	100.0	4.6105 - 4.5588

4. Conclusions

A high-entropy carbide was formed through the reaction between a ZrNbHfTa foil and graphite. The metal to carbide conversion was completed in a 16 s flash treatment with the maximum temperature exceeding 2200 °C.

The first carbide formed from the reaction between ZrNbHfTa and graphite was rich in Hf and Zr, and poor in Ta and Nb. This was consistent with the thermochemical data in the literature, showing that Hf and Zr have a larger negative free energy for carbide formation than Ta and Nb.

The heating rate highly impacted on the final microstructure. As a matter of fact, flash treatments allowed melting, deformation and squeezing of the alloy interlayer before it reacted with the graphite. On the contrary, in the case of slow heating rates with SPS (i.e., 10 °C/min), the interlayer conversion to carbide had been completed before it melted or became plastically deformable. This concept is general and can be likely applied to different metal/graphite systems.

Acknowledgements

This material is based upon work supported by the Air Force Office of Scientific Research under award number FA9550-17-1-0526.

The authors gratefully acknowledge the JECS Trust for funding the visit of M. Biesuz to the Queen Mary University of London (Contract No. 2018172).

References

[1] C.M. Rost, E. Sachet, T. Borman, A. Moballegh, E.C. Dickey, D. Hou, J.L. Jones, S. Curtarolo, J.-P. Maria, Entropy-stabilized oxides, Nat. Commun. 6 (2015) 8485. doi:10.1038/ncomms9485.

[2] Z. Rak, C.M. Rost, M. Lim, P. Sarker, C. Toher, S. Curtarolo, J.P. Maria, D.W. Brenner, Charge compensation and electrostatic transferability in three entropy-stabilized oxides: Results from density functional theory calculations, J. Appl. Phys. 120 (2016) 095105. doi:10.1063/1.4962135.

[3] D. Bérardan, S. Franger, D. Dragoe, A.K. Meena, N. Dragoe, Colossal dielectric constant in high entropy oxides, Phys. Status Solidi - Rapid Res. Lett. 10 (2016) 328–333. doi:10.1002/pssr.201600043.

[4] J. Gild, Y. Zhang, T. Harrington, S. Jiang, T. Hu, M.C. Quinn, W.M. Mellor, N. Zhou, K. Vecchio, J. Luo, High-Entropy Metal Diborides: A New Class of High-Entropy Materials and a New Type of Ultrahigh Temperature Ceramics, Sci. Rep. 6 (2016) 37946. http://www.nature.com/articles/srep37946.

[5] A. Sarkar, R. Djenadic, N.J. Usharani, K.P. Sanghvi, V.S.K. Chakravadhanula, A.S. Gandhi, H. Hahn, S.S. Bhattacharya, Nanocrystalline multicomponent entropy stabilised transition metal oxides, J. Eur. Ceram. Soc. 37 (2017) 747–754. http://dx.doi.org/10.1016/j.jeurceramsoc.2016.09.018.

[6] M. Biesuz, L. Spiridigliozzi, G. Dell'Agli, M. Bortolotti, V.M. Sglavo, Synthesis and sintering of (Mg, Co, Ni, Cu, Zn)O entropy-stabilized oxides obtained by wet chemical methods, J. Mater. Sci. 53 (2018) 8074–8085. doi:10.1007/s10853-018-2168-9.

[7] J. Gild, M. Samiee, J.L. Braun, T. Harrington, H. Vega, P.E. Hopkins, K. Vecchio, J. Luo, High-entropy fluorite oxides, J. Eur. Ceram. Soc. 38 (2018) 3578–3584. doi:10.1016/j.jeurceramsoc.2018.04.010.

[8] A.D. Dupuy, X. Wang, J.M. Schoenung, Entropic phase transformation in nanocrystalline high entropy oxides Entropic phase transformation in nanocrystalline high entropy oxides, Mater. Res. Lett. 7 (2019) 60–67. doi:10.1080/21663831.2018.1554605.

[9] A. Mao, H.-Z. Xiang, Z.-G. Zhang, K. Kuramoto, H. Yu, S. Ran, Solution combustion synthesis and magnetic property of rock-salt (Co0.2Cu0.2Mg0.2Ni0.2Zn0.2)O high-entropy oxide nanocrystalline powder, J. Magn. Magn. Mater. 484 (2019) 245–252. doi:10.1016/j.jmmm.2019.04.023.

[10] R. Zhang, M.J. Reece, Review of high entropy ceramics: design, synthesis, structure and properties, J. Mater. Chem. A. (2019) 22148–22162. doi:10.1039/c9ta05698j.

[11] D. Bérardan, S. Franger, A.K. Meena, N. Dragoe, Room temperature lithium superionic conductivity in high entropy oxides, J. Mater. Chem. A. 4 (2016) 9536–9541. doi:10.1039/C6TA03249D.

[12] H. Chen, J. Fu, P. Zhang, H. Peng, C.W. Abney, K. Jie, X. Liu, M. Chi, S. Dai, Entropy-stabilized metal oxide solid solutions as CO oxidation catalysts with high-temperature stability, J.

Mater. Chem. A. 6 (2018) 11129–11133. doi:10.1039/C8TA01772G.

[13] E. Castle, T. Csanádi, S. Grasso, J. Dusza, M. Reece, Processing and Properties of High-Entropy Ultra-High Temperature Carbides, Sci. Rep. 8 (2018) 8609. doi:10.1038/s41598-018-26827-1.

[14] P. Malinovskis, S. Fritze, L. Riekehr, L. Von Fieandt, J. Cedervall, D. Rehnlund, L. Nyholm, E. Lewin, U. Jansson, Synthesis and characterization of multicomponent (CrNbTaTiW) C fi lms for increased hardness and corrosion resistance, Mater. Des. 149 (2018) 51–62. doi:10.1016/j.matdes.2018.03.068.

[15] J. Zhou, J. Zhang, F. Zhang, B. Niu, L. Lei, W. Wang, High-entropy carbide : A novel class of multicomponent ceramics, Ceram. Int. 44 (2018) 22014–22018. doi:10.1016/j.ceramint.2018.08.100.

[16] T.J. Harrington, J. Gild, P. Sarker, C. Toher, C.M. Rost, O.F. Dippo, C. Mcelfresh, K. Kaufmann, E. Marin, L. Borowski, P.E. Hopkins, J. Luo, S. Curtarolo, D.W. Brenner, K.S. Vecchio, Phase stability and mechanical properties of novel high entropy transition metal carbides, Acta Mater. 166 (2019) 271–280. doi:10.1016/j.actamat.2018.12.054.

[17] P. Sarker, T. Harrington, C. Toher, C. Oses, M. Samiee, J. Maria, D.W. Brenner, K.S. Vecchio, S. Curtarolo, High-entropy high-hardness metal carbides discovered by entropy descriptors, Nat. Commun. 9 (2018) 4980. doi:10.1038/s41467-018-07160-7.

[18] J. Dusza, Š. Peter, V. Girman, R. Sedlák, E.G. Castle, T. Csanádi, A. Koval, M.J. Reece, Microstructure of (Hf-Ta-Zr-Nb) C high-entropy carbide at micro and nano / atomic level, J. Eur. Ceram. Soc. 38 (2018) 4303–4307. doi:10.1016/j.jeurceramsoc.2018.05.006.

[19] Q. Zhang, J. Zhang, L. Neng, W. Chen, Understanding the electronic structure , mechanical properties , and thermodynamic stability of (TiZrHfNbTa) C combined experiments and first-principles simulation Understanding the electronic structure , mechanical properties , and thermodynamic stabil, J. Appl. Phys. 126 (2019) 025101. doi:10.1063/1.5094580.

[20] M. Patel, V. Singh, S. Singh, V. V. Bhanu Prasad, Micro-structural evolution during diffusion bonding of C-SiC/C-SiC composite using Ti interlayer, Mater. Charact. 135 (2018) 71–75. doi:10.1016/j.matchar.2017.11.031.

[21] M. Ferraris, M. Salvo, C. Isola, M. Appendino Montorsi, a. Kohyama, Glass-ceramic joining and coating of SiC/SiC for fusion applications, J. Nucl. Mater. 258–263 (1998) 1546–1550. doi:10.1016/S0022-3115(98)00176-7.

[22] S.J. Glass, F.M. Mahoney, B. Quillan, J.P. Pollinger, R.E. Loehman, Refractory oxynitride joints in silicon nitride, Acta Mater. 46 (1998) 2393–2399. doi:10.1016/S1359-6454(98)80021-9.

[23] R. Chaim, B.G. Ravi, Joining of alumina ceramics using nanocrystalline tape cast interlayer, J. Mater. Res. 15 (2000) 1724–1728.

[24] B.G. Ravi, R. Chaim, Joining of ZrO 2 -4 .5 wt % Y2O3 (Y-TZP) ceramics using nanocrystalline tape cast interlayers, J. Mater. Sci. 37 (2002) 813–818.

[25] D.H. Jeong, A. Septiadi, P. Fitriani, D.H. Yoon, Joining of SiCf/SiC using polycarbosilane and

polysilazane preceramic mixtures, Ceram. Int. 44 (2018) 10443–10450. doi:10.1016/j.ceramint.2018.03.061.

[26] P. Colombo, G. Mera, R. Riedel, G.D. Sorarù, Polymer-derived ceramics: 40 Years of research and innovation in advanced ceramics, J. Am. Ceram. Soc. 93 (2010) 1805–1837. doi:10.1111/j.1551-2916.2010.03876.x.

[27] P. Colombo, V. Sglavo, E. Pippel, P. Colombo, Joining of reaction-bonded silicon carbide using a preceramic polymer, J. Mater. Sci. 33 (1998) 2405–2412. doi:10.1023/A:1004312109836.

[28] S. Rizzo, S. Grasso, M. Salvo, V. Casalegno, M.J. Reece, M. Ferraris, Joining of C/SiC composites by spark plasma sintering technique, J. Eur. Ceram. Soc. 34 (2014) 903–913. doi:10.1016/j.jeurceramsoc.2013.10.028.

[29] E.J. Pickering, N.G. Jones, High-entropy alloys: a critical assessment of their founding principles and future prospects, Int. Mater. Rev. 61 (2016) 183–202. doi:10.1080/09506608.2016.1180020.

[30] D.B. Miracle, O.N. Senkov, A critical review of high entropy alloys and related concepts, Acta Mater. 122 (2017) 448–511. doi:10.1016/j.actamat.2016.08.081.

[31] T. Te Chou, W.H. Tuan, H. Nishikawa, B.J. Weng, Brazing Graphite to Aluminum Nitride for Thermal Dissipation Purpose, Adv. Eng. Mater. 19 (2017) 5–10. doi:10.1002/adem.201600876.

[32] L. Xing, J. Lin, M. Huang, W. Yang, Joining of Graphite to Copper with Nb Interlayer: Microstructure and Mechanical Properties, Adv. Eng. Mater. 1800810 (2018) 1–8. doi:10.1002/adem.201800810.

[33] Y. Mao, L. Peng, S. Wang, L. Xi, Microstructural characterization of graphite/CuCrZr joints brazed with CuTiH2Ni-based fillers, J. Alloys Compd. 716 (2017) 81–87. doi:10.1016/j.jallcom.2017.05.019.

[34] M. Cologna, B. Rashkova, R. Raj, Flash sintering of nanograin zirconia in <5 s at 850°C, J. Am. Ceram. Soc. 93 (2010) 3556–3559.

[35] B. Mattan Ze'ev, N. Shomrat, Y. Tsur, Recent Advances in Mechanism Research and Methods for Electric-Field-Assisted Sintering of Ceramics, Adv. Mater. 30 (2018) 1706369. doi:10.1002/adma.201706369.

[36] M. Yu, S. Grasso, R. Mckinnon, T. Saunders, M.J. Reece, Review of flash sintering: materials, mechanisms and modelling, Adv. Appl. Ceram. 116 (2017) 24–60. doi:10.1080/17436753.2016.1251051.

[37] M. Biesuz, V.M. Sglavo, Flash sintering of ceramics, J. Eur. Ceram. Soc. 39 (2019) 115–143. doi:10.1016/j.jeurceramsoc.2018.08.048.

[38] S. Grasso, T. Saunders, H. Porwal, B. Milsom, A. Tudball, M. Reece, Flash Spark Plasma Sintering (FSPS) of alpha and beta SiC, J. Am. Ceram. Soc. 99 (2016) 1534–1543. doi:10.1111/jace.14158.

[39] S. Grasso, T. Saunders, H. Porwal, O. Cedillos-Barraza, D.D. Jayaseelan, W.E. Lee, M.J. Reece, Flash spark plasma sintering (FSPS) of pure ZrB2, J. Am. Ceram. Soc. 97 (2014) 2405–2408. doi:10.1111/jace.13109.

[40] R.I. Todd, E. Zapata-Solvas, R.S. Bonilla, T. Sneddon, P.R. Wilshaw, Electrical characteristics of flash sintering: Thermal runaway of Joule heating, J. Eur. Ceram. Soc. 35 (2015) 1865–1877. doi:10.1016/j.jeurceramsoc.2014.12.022.

[41] W. Ji, B. Parker, S. Falco, J.Y. Zhang, Z.Y. Fu, R.I. Todd, Ultra-fast firing: Effect of heating rate on sintering of 3YSZ, with and without an electric field, J. Eur. Ceram. Soc. 37 (2017) 2547–2551.

[42] R. Chaim, Liquid film capillary mechanism for densification of ceramic powders during flash sintering, Materials (Basel). 9 (2016) 19–21. doi:10.3390/ma9040280.

[43] M. Biesuz, D. Rizzi, V.M. Sglavo, Electric current effect during the early stages of field-assisted sintering, J. Am. Ceram. Soc. 102 (2019) 813–822. doi:10.1111/jace.15976.

[44] D. Liu, Y. Cao, J. Liu, Y. Gao, Y. Wang, Effect of oxygen partial pressure on temperature for onset of flash sintering 3YSZ, J. Eur. Ceram. Soc. 38 (2018) 817–820. doi:10.1016/j.jeurceramsoc.2017.09.009.

[45] M. Biesuz, L. Pinter, T. Saunders, M. Reece, J. Binner, V.M. Sglavo, S. Grasso, Investigation of Electrochemical, Optical and Thermal Effects during Flash Sintering of 8YSZ, Materials (Basel). 11 (2018) 1214. doi:10.3390/ma11071214.

[46] X. Vendrell, A.R. West, Induced p- type semi-conductivity in yttria-stabilised zirconia, J. Am. Ceram. Soc. IN PRESS (2019). doi:10.1111/jace.16492.

[47] R. Shi, Y. Pu, J. Li, X. Guo, W. Wang, M. Yang, Y. Shi, Particle transport mode during fl ash sintering of sodium bismuth titanate ceramic, Ceram. Int. IN PRESS (2019). doi:10.1016/j.ceramint.2019.04.015.

[48] T. Prasad, V. Avila, R. Roberto, I. Neto, M. Bram, O. Guillon, R. Raj, On the role of Debye temperature in the onset of fl ash in three oxides, Scr. Mater. 170 (2019) 81–84. doi:10.1016/j.scriptamat.2019.05.030.

[49] J. Gonzalez-Julian, K. Jahnert, K. Speer, L. Liu, J. Rathel, M. Knapp, H. Ehrenberg, M. Bram, O. Guillon, Effect of Internal Current Flow during the Sintering of Zirconium Diboride by Field Assisted Sintering Technology, J. Am. Ceram. Soc. 99 (2016) 35–42. doi:10.1111/jace.13931.

[50] C. Schmerbauch, J. Gonzalez-Julian, R. Röder, C. Ronning, O. Guillon, Flash sintering of nanocrystalline zinc oxide and its influence on microstructure and defect formation, J. Am. Ceram. Soc. 97 (2014) 1728–1735. doi:10.1111/jace.12972.

[51] L.M. Jesus, R.S. Silva, R. Raj, J.-C. M'Peko, Electric field-assisted ultrafast synthesis of nanopowders: a novel and cost-efficient approach, RSC Adv. 6 (2016) 107208–107213. doi:10.1039/C6RA18734J.

[52] N. Morisaki, H. Yoshida, K. Matsui, T. Tokunaga, K. Sasaki, T. Yamamoto, Synthesis of zirconium oxynitride in air under DC electric fields, Appl. Phys. Lett. 109 (2016) 083104.

[53] D. Kok, S.K. Jha, R. Raj, M.L. Mecartney, Flash sintering of a three-phase alumina, spinel, and yttria-stabilized zirconia composite, J. Am. Ceram. Soc. (2017) 16–19. doi:10.1111/jace.14818.

[54] B. Yoon, D. Yadav, S. Ghose, P. Sarin, R. Raj, E. Program, On the Synchronicity of Flash Sintering and Phase Transformation, 2019. (n.d.) IN PRESS. doi:10.1111/jace.16335.

[55] E. Gil-González, A. Perejón, P.E. Sánchez-Jiménez, M.J. Sayagués, R. Raj, L.A. Pérez-Maqueda, Phase-pure BiFeO3 produced by reaction flash-sintering of Bi2O3 and Fe2O3, Mater. Chem. A. 6 (2018) 5356–5366. doi:10.1039/C7TA09239C.

[56] C. McLaren, W. Heffner, R. Tessarollo, R. Raj, H. Jain, Electric field-induced softening of alkali silicate glasses, Appl. Phys. Lett. 107 (2015) 1–6. doi:10.1063/1.4934945.

[57] C.T. Mclaren, C. Kopatz, N.J. Smith, H. Jain, Development of highly inhomogeneous temperature profile within electrically heated alkali silicate glasses, Sci. Rep. 9 (2019) 2805. doi:10.1038/s41598-019-39431-8.

[58] P. Tatarko, S. Grasso, T.G. Saunders, V. Casalegno, M. Ferraris, M.J. Reece, Flash joining of CVD-SiC coated C f /SiC composites with a Ti interlayer, J. Eur. Ceram. Soc. 37 (2017) 3841–3848.

[59] X. Zhao, L. Duan, Y. Wang, Fast interdiffusion and Kirkendall effects of SiC-coated C/SiC composites joined by a Ti-Nb-Ti interlayer via spark plasma sintering, J. Eur. Ceram. Soc. (2019) 0–1. doi:10.1016/j.jeurceramsoc.2019.01.020.

[60] J. Xia, K. Ren, Y. Wang, Reversible joining of zirconia to titanium alloy, Ceram. Int. 45 (2018) 2509–2515. doi:10.1016/j.ceramint.2018.10.180.

[61] J. Xia, K. Ren, Y. Wang, L. An, Reversible flash-bonding of zirconia and nickel alloys, Scr. Mater. 153 (2018) 31–34. doi:10.1016/j.scriptamat.2018.04.047.

[62] J. Xia, K. Ren, Y. Wang, One-second fl ash joining of zirconia ceramic by an electric fi eld at low temperatures, Scr. Mater. 165 (2019) 34–38. doi:10.1016/j.scriptamat.2019.02.004.

[63] J. Xia, K. Ren, W. Liu, Y. Wang, Ultrafast joining of zirconia ceramics using electric fi eld at low temperatures, J. Eur. Ceram. Soc. IN PRESS (2019). doi:10.1016/j.jeurceramsoc.2019.04.023.

[64] J. Gild, K. Kaufmann, K. Vecchio, J. Luo, Reactive fl ash spark plasma sintering of high-entropy ultrahigh temperature ceramics, Scr. Mater. 170 (2019) 106–110. doi:10.1016/j.scriptamat.2019.05.039.

[65] O.N. Senkov, J.M. Scott, S.V. Senkova, D.B. Miracle, C.F. Woodward, Microstructure and room temperature properties of a high-entropy TaNbHfZrTi alloy, J. Alloys Compd. 509 (2011) 6043–6048. doi:10.1016/j.jallcom.2011.02.171.

[66] L. Lilensten, J.-P. Couzinié, L. Perrière, A. Hocini, C. Keller, G. Dirras, I. Guillot, Study of a bcc multi-principal element alloy: Tensile and simple shear properties and underlying deformation mechanisms, Acta Mater. 142 (2018) 131–141. doi:10.1016/j.actamat.2017.09.062.

[67] L. Lutterotti, M. Bortolotti, G. Ischia, I. Lonardelli, H.-R. Wenk, Rietveld texture analysis from diffraction images, Zeitschrift Fur Krist. Suppl. 1 (2007) 125–130.

[68] R. Young, The Rietveld Method, By RA Young, Oxford Univ. Press. Oxford. (1993) 312. doi:10.1017/CBO9781107415324.004.

[69] S. Matthies, J. Pehl, H.R. Wenk, L. Lutterotti, S.C. Vogel, Quantitative texture analysis with the HIPPO neutron TOF diffractometer, J. Appl. Crystallogr. 38 (2005) 462–475. doi:10.1107/S0021889805006187.

[70] T. Saunders, P. Tatarko, S. Grasso, M.J. Reece, Effectiveness of boria welding fl ux in improving the wettability of ZrB 2 in contact with molten Cu, J. Eur. Ceram. Soc. 38 (2018) 4198–4202. doi:10.1016/j.jeurceramsoc.2018.04.059.

[71] J.Q. Yao, X.W. Liu, N. Gao, Q.H. Jiang, N. Li, G. Liu, W.B. Zhang, Z.T. Fan, Intermetallics refractory high-entropy alloy, Intermetallics. 98 (2018) 79–88. doi:10.1016/j.intermet.2018.04.023.

[72] O.N. Senkov, J.M. Scott, S. V Senkova, D.B. Miracle, C.F. Woodward, Microstructure and room temperature properties of a high-entropy TaNbHfZrTi alloy, J. Alloys Compd. 509 (2011) 6043–6048. doi:10.1016/j.jallcom.2011.02.171.

[73] A. Meden, S. Maiti, W. Steurer, M. Feuerbacher, J. Dolin, Superconductivity in thermally annealed Ta-Nb-Hf-Zr-Ti high-entropy alloys, J. Alloys Compd. 695 (2017) 3530–3540. doi:10.1016/j.jallcom.2016.11.417.

[74] J.P. Couzinié, G. Dirras, L. Perrière, T. Chauveau, E. Leroy, Y. Champion, I. Guillot, Microstructure of a near-equimolar refractory high-entropy alloy, Mater. Lett. 126 (2014) 285–287. doi:10.1016/j.matlet.2014.04.062.

[75] M. Feuerbacher, M. Heidelmann, C. Thomas, Plastic deformation properties of Zr – Nb – Ti – Ta – Hf high-entropy alloys, Philos. Mag. 95 (2015) 1222–1233. doi:10.1080/14786435.2015.1028506.

[76] G. Dirras, L. Lilensten, P. Djemia, M. Laurent-brocq, D. Tingaud, J. Couzinié, L. Perrière, T. Chaveau, I. Guillot, Elastic and plastic properties of as-cast equimolar TiHfZrTaNb high-entropy alloy, Mater. Sci. Eng. A. 654 (2016) 30–38. doi:10.1016/j.msea.2015.12.017.

[77] S. Ji, I. Chang, Y.H. Lee, J. Park, J.Y. Paek, M.H. Lee, S.W. Cha, Fabrication of low-temperature solid oxide fuel cells with a nanothin protective layer by atomic layer deposition, Nanoscale Res. Lett. Lett. 8 (2013) 1–7.

[78] M.T. Marques, A.M. Ferraria, J.B. Correia, A.M. Botelho, R. Vilar, XRD , XPS and SEM characterisation of Cu – NbC nanocomposite produced by mechanical alloying, Mater. Chem. Phys. 109 (2008) 174–180. doi:10.1016/j.matchemphys.2007.10.032.

[79] L. Wang, J. Sun, B. Kang, S. Li, S. Ji, Z. Wen, X. Wang, Electrochemical behaviour and surface conductivity of niobium carbide-modi fi ed austenitic stainless steel bipolar plate, J. Power Sources. 246 (2014) 775–782. doi:10.1016/j.jpowsour.2013.08.025.

[80] F. Piallat, V. Beugin, R. Gassilloud, P. Michallon, L. Dussault, B. Pelissier, T. Asikainen, J. Willem, F. Martin, P. Morin, C. Vallée, Microelectronic Engineering Evaluation of plasma

parameters on PEALD deposited TaCN, Microelectron. Eng. 107 (2013) 156–160. doi:10.1016/j.mee.2012.08.020.

[81] J. Yang, Z. Liu, H. Wang, K. Xiao, Q. Guo, J. Song, L. Liu, The reaction behavior of carbon fibers and TaC at high temperatures, CrystEngComm. 15 (2013) 6928–6931. doi:10.1039/c3ce40463c.

[82] Y. Chang, H. Huang, Y. Chen, J. Hsu, T. Shieh, M. Tsai, Biological Characteristics of the MG-63 Human Osteosarcoma Cells on Composite Tantalum Carbide / Amorphous Carbon Films, PLoS One. 9 (2014) e95590. doi:10.1371/journal.pone.0095590.

[83] M. Qi, J. Xiao, C. Gong, A. Jiang, Y. Chen, Evolution of the mechanical and tribological properties of DLC thin films doped with low-concentration hafnium on 316L steel, J. Phys. D. Appl. Phys. 51 (2018) 025301.

[84] K. Hans, S. Latha, P. Bera, H.C. Barshilia, Hafnium carbide based solar absorber coatings with high spectral selectivity, Sol. Energy Mater. Sol. Cells. 185 (2018) 1–7. doi:10.1016/j.solmat.2018.05.005.

[85] A. Singh, M.H. Modi, A.K. Sinha, R. Dhawan, G.S. Lodha, Study of structural and optical properties of zirconium carbide (ZrC) thin- fi lms deposited by ion beam sputtering for soft x-ray optical applications, Surf. Coat. Technol. 272 (2015) 409–414. doi:10.1016/j.surfcoat.2015.03.033.

[86] I. Barin, Thermochemical data of pure substances, III, VCH Verlagsgesellschaft mbH and VCH Publishers, Inc., Weinheim, Federal Republic of Germany, 1995.

[87] Z. Wang, I. Baker, W. Guo, J.D. Poplawsky, The effect of carbon on the microstructures, mechanical properties, and deformation mechanisms of thermo-mechanically treated Fe40.4Ni11.3Mn34.8Al7.5Cr6 high entropy alloys, Acta Mater. 126 (2017) 346–360. doi:10.1016/j.actamat.2016.12.074.

[88] S. Fang, W. Chen, Z. Fu, Microstructure and mechanical properties of twinned Al0.5CrFeNiCo0.3C0.2 high entropy alloy processed by mechanical alloying and spark plasma sintering, Mater. Des. 54 (2014) 973–979. doi:10.1016/j.matdes.2013.08.099.

[89] M. Laurent-Brocq, P.-A. Goujon, J. Monnier, B. Villeroy, L. Perrière, R. Pirès, G. Garcin, Microstructure and mechanical properties of a CoCrFeMnNi high entropy alloy processed by milling and spark plasma sintering, J. Alloys Compd. 780 (2019) 856–865. doi:10.1016/j.jallcom.2018.11.181.